

Properties of the post in-spiral common envelope ejecta II: dust formation

Roberto Iaconi^{1*} †, Keiichi Maeda¹, Takaya Nozawa², Orsola De Marco^{3,4}
and Thomas Reichardt^{3,4}

¹*Department of Astronomy, Kyoto University, Kitashirakawa-Oiwake-cho, Sakyo-ku, Kyoto 606-8502, Japan 0000-0002-1940-1950*

²*Division of Theoretical Astronomy, National Astronomical Observatory of Japan, Mitaka, Tokyo 181-8588, Japan*

³*Department of Physics & Astronomy, Macquarie University, Sydney, NSW 2109, Australia*

⁴*Astronomy, Astrophysics and Astrophotonics Research Centre, Macquarie University, Sydney, NSW 2109, Australia*

Submitted to MNRAS, 26 May 2022

ABSTRACT

We study the formation of dust in the expanding gas ejected as a result of a common envelope binary interaction. In our novel approach, we apply the dust formation model of Nozawa et al. to the outputs of the 3D hydrodynamic SPH simulation performed by Iaconi et al., that involves a giant of $0.88 M_{\odot}$ and $83 R_{\odot}$, with a companion of $0.6 M_{\odot}$ placed on the surface of the giant in circular orbit. After simulating the dynamic in-spiral phase we follow the expansion of the ejecta for $\simeq 18\,000$ days. During this period the gas is able to cool down enough to reach dust formation temperatures. Our results show that dust forms efficiently in the window between $\simeq 300$ days (the end of the dynamic in-spiral) and $\simeq 5000$ days. The dust forms in two separate populations; an outer one in the material ejected during the first few orbits of the companion inside the primary's envelope and an inner one in the rest of the ejected material. The inner dust population dominates the grain size distribution at the end of the simulation. We are able to fit the grain size distribution at the end of the simulation with a double power law. The slope of the power law for smaller grains is flatter than that for larger grains, creating a knee-shaped distribution. The power law indexes are however different from the classical values determined for the interstellar medium. We also estimate that the contribution to cosmic dust by common envelope events is not negligible and comparable to that of novae and supernovae.

Key words: stars: evolution - binaries: close - hydrodynamics - methods: analytic, numerical - dust, extinction

1 INTRODUCTION

The common envelope interaction (Paczynski 1976, Ivanova et al. 2013; hereafter CE) is a binary interaction process that leads to a reduction in a binary's orbital separation resulting in a merger or in the formation of compact evolved binaries, which in turn can become Type Ia supernovae, gamma-ray bursts, or merging double black holes or neutron stars emitting detectable gravitational waves. A typical common envelope configuration is a giant primary and a more compact companion, such as a main sequence star or a white dwarf but other configurations are possible.

Given its intrinsic three-dimensional structure and physical complexity research on CE has been mainly carried out through hydrodynamic simulations. Several simulations have been performed

with different codes (e.g., Sandquist et al. 1998, Ricker & Taam 2012, Passy et al. 2012 and Ohlmann et al. 2016a, to cite a few; see table A3 of Iaconi & De Marco 2019 for a complete list). Different physical mechanisms and their impact on the final outcome have been considered: H and He recombination energy injected in the gas when the envelope expands and cools down (Nandez et al. 2015, Nandez & Ivanova 2016, Ivanova & Nandez 2016, Soker et al. 2018, Ivanova 2018), the magnetic field generated by the companion star (Ohlmann et al. 2016b), jets from the companion star (Shiber et al. 2017, Shiber & Soker 2018, Shiber et al. 2019, Schreier et al. 2019, López-Cámara et al. 2019), pre-CE Roche lobe overflow (Reichardt et al. 2019b), envelope fall-back (Kurwita et al. 2016), high orbital eccentricities (Staff et al. 2016), dust-driven winds (Glanz & Perets 2018), stellar pulsations (Clayton et al. 2017), convection (Wilson & Nordhaus 2019). CE wind tunnel simulations have also been carried out by MacLeod et al. (2017), Murguía-Berthier et al. (2017) and De et al. (2019). All these works analyse the dynamic in-spiral phase, during which the

* email: roberto.iaconi@kustastro.kyoto-u.ac.jp

† JSPS International Research Fellow (Graduate School of Science, Kyoto University)

two stars quickly approach each other in a time-scale comparable to the dynamical time-scale of the primary, i.e., from months to years.

This paper follows on from Iaconi et al. (2019), where we analysed the behaviour of the CE ejecta after the dynamic in-spiral. We carried out a 3D SPH simulation almost identical to those of Iaconi et al. (2018), but we ran the simulation for longer, 18 434 days ($\simeq 50$ yr) after the end of the dynamic in-spiral and analysed the dynamic and thermodynamic properties of the extended envelope gas. In that paper we showed that the evolution of the CE ejecta, after the termination of the dynamic in-spiral, can be approximated by homologous expansion after $\simeq 5000$ days from the beginning of the simulation (the end of in-spiral is at $\simeq 300$ days). We also observed the formation of ring-like features expanding self-similarly. If the post dynamic in-spiral CE evolution is homologous, then it can be fully calculated analytically by applying the homologous expansion equations to any simulation data dump chosen as initial conditions. We showed the power of this approach by building a toy model for the calculation of the photosphere where the ejecta expand following the homologous dynamics and the main contribution to opacity is provided by dust formed in the cooling envelope gas. The determination of the photosphere location and temperature carried in Iaconi et al. (2019) did not explain in detail how the calculations of the dust formation were performed, something that we concentrate on here.

A model for dust formation in CE ejecta was previously carried out by Lü et al. (2013). Their model presents some substantial differences with respect to ours. First, they assume that the CE ejecta expand following the kinematics of a stellar wind with spherical symmetry. Second, they considered olivine-type silicates, pyroxene-type silicates and iron grains, while we utilise the pyroxene-type silicate MgSiO_3 and carbon grains. Finally, Lü et al. (2013) adopted the dust formation model by Ferrarotti & Gail (2006), who specify the number of seed nuclei by hand, while we use the dust formation model by Nozawa & Kozasa (2013), which treats seed formation and dust growth self-consistently. Dust formation in common envelopes was also considered analytically by Glanz & Perets (2018), who explore the idea that dust-driven winds taking place after the dynamic in-spiral might help to unbind the envelope. Our study, on the other hand, is the first that presents a detailed model of dust formation in CE ejecta based on the outputs of 3D SPH hydrodynamic simulations (we also highlight that, even in other astrophysical contexts, e.g., supernovae, only a few studies of dust formation applied to 3D simulations have been performed). Dust formation does not happen at fixed locations but is achieved in the flow of the gas parcels. Therefore, grid-based hydrodynamic codes, which use Eulerian schemes, can be coupled to dust formation models only by introducing a large number of test particles. Such kind of approach results in approximations. On the other hand, this study uses an SPH code, based on a Lagrangian formalism, which allows us to follow every moving element of the fluid without any approximation.

This paper is structured as follows: in Section 2 we describe the dust formation model we use and how we applied it to our data; in Section 3 we describe the process of dust formation; in Section 4 we show the main characteristics of the dust grains that form in the ejected envelope (grains size, location, mass, size distribution and contribution to the cosmic dust); in Section 5 we compare our results with the observations of dust in the post-CE system V1309 Sco. Finally, the summary and conclusions are given in Section 6.

2 DUST FORMATION MODEL

In this section we give an explanation of the dust formation model and how we applied it to our data. For a full description of the model, see Nozawa & Kozasa (2013).

2.1 Model description

Nozawa & Kozasa (2013) formulated the non-steady-state dust formation process involving nucleation and grain growth, and applied it to two grain species: pyroxene-type silicates (MgSiO_3) and carbon (C). The choice is based on the fact that these are considered to be the most representative species of dust grains in the interstellar space. Which one between C and MgSiO_3 grains is formed is determined by the number ratio of carbon and oxygen atoms in the gas phase (hereafter referred to as the C/O ratio). It has been considered that the abundances of gaseous C and O atoms are mainly controlled by the formation of CO molecules, because CO molecules efficiently form at relatively high temperatures and almost completely trap either C or O atoms prior to dust formation, depending on which one has a lower number density. Let us consider the conditions required for the formation of the two types of dust separately.

MgSiO_3 grains are the most expected type of dust in a situation like the one we simulate here. Our dust formation calculations are in fact based on the ejecta properties of a CE involving a RGB star, where we assume solar abundances (Asplund et al. 2009; where the number fractions of the elements forming the two types of grains decrease in the following order: $n_{\text{O}} > n_{\text{C}} > n_{\text{Mg}} > n_{\text{Si}}$). Thus, the fact that RGB stars tend to have a C/O ratio smaller than unity, because they have not yet experienced the third dredge up, results in all the C atoms to be most likely locked up in CO molecules. This prevents the formation of C grains, leaving the MgSiO_3 grains to be the main dust species formed.

Nevertheless, we still consider the formation of C grains in our CE ejecta. Indeed there have been suggestions that CO molecules can be easily destroyed by energetic electrons, which enables, even for $\text{C/O} < 1$, the condensation of C grains from gas-phase C atoms that are not bound in CO molecules (Clayton et al. 1999). In addition, observations of classic novae have revealed the concurrent formation of silicate and carbon grains in their ejecta (Evans et al. 2005, Sakon et al. 2016). These works indicate that the formation of CO molecules is not always complete, and that C grains can condense in the ejected gas with $\text{C/O} < 1$. Hence, we also address the formation of C grains under the extreme assumption that no CO molecule is formed. We note that investigating the formation of C grains in the context of this study can be considered as probing the dust formation in C-rich CE ejecta as expected if the primary stars are asymptotic giant branch (AGB) stars.

For both of the grain species, the amount of dust that forms depends on the abundance of elements that can solidify into dust. Generally for MgSiO_3 grains, Si atoms are assumed to combine with O to form SiO molecules, whose abundance is equal to that of the Si atoms. Therefore, the amount of MgSiO_3 grains formed is proportional to the least abundant element between Mg and Si. In our case, it is Si, which we will use as the key species for all the calculations related to MgSiO_3 grains. For C grains the key species is simply C, which we will use as the key species for the related calculations.

2.2 Application of the dust model to the common envelope simulation outputs

The condensation of dust takes place in the cooling gas, where the unsaturated state turns into the supersaturated state determined by the condition $S > 1$, where S is the supersaturation ratio of the gas (equation 56 of Nozawa & Kozasa 2013). Thus, to determine if dust condensation takes place, we need to follow the supersaturation ratio, which depends on the temperature and partial pressure of condensible gaseous atoms (Nozawa & Kozasa 2013). Our hydrodynamic simulations of the CE ejecta record the density and pressure (which can be converted to temperature), as a function of time for each SPH particle. Hence, the feasibility of dust formation can be assessed, based on the evolution of S calculated from the simulation outputs.

Nozawa & Kozasa (2013) found that the formation of MgSiO_3 and C grains in the expanding gas can be achieved when the non-dimensional quantity $\Lambda_{\text{on}} = \tau_{\text{sat}}(t_{\text{on}})/\tau_{\text{coll}}(t_{\text{on}})$ is higher than unity, where τ_{sat} is the time-scale in which the supersaturation ratio increases, τ_{coll} is the time-scale on which the gas particles collide, and t_{on} is the onset time of dust formation; Λ_{on} represents the ratio of time-scales between the seed nuclei formation and grain growth at t_{on} . Note that the supersaturation ratio increases with decreasing the gas temperature by roughly following the relation $\ln S \propto T^{-1}$. Hence, S is sensitive to gas temperature T , and $\tau_{\text{sat}} = |d \ln S / dt|^{-1}$ is approximately proportional to the cooling time of the gas.

Nozawa & Kozasa (2013) also showed that the typical radius of newly formed dust can be determined by the value of Λ_{on} . In this study, we examine the possibility of dust formation, and estimate the size and mass of dust by calculating Λ_{on} for each SPH particle and for the entire duration of the simulation. In our calculations, the onset time of dust formation t_{on} is defined as the time when S reaches 10. The gas temperatures when $S = 10$ are $\simeq 1200$ – 1600 K and $\simeq 1700$ – 2100 K for MgSiO_3 and C grains, respectively, depending on the number density of the key gas species. Since the time-scale of dust formation (a few days) is much shorter than the dynamical time-scale of the ejecta, t_{on} can be regarded as the condensation time of dust.

In Iaconi et al. (2019), the formula we used to calculate Λ_{on} assumed homologous evolution of the density and temperature of the gas. This assumption affects the value of Λ_{on} , since the time-scale of gas cooling is regulated by the time-scale of gas expansion. However, our simulation reveals that the evolution of the ejecta can be described by an homologous model only after $\simeq 5000$ days. In this sense, Iaconi et al. (2019) made rough estimates of the formation time and size of dust formed in CE ejecta. In this study, we remove the assumption of the homologous expansion for the evolution of density and temperature, and we derive Λ_{on} directly and independently for each SPH particle on the basis of the time-scale of gas cooling obtained from the temperature derivative between one code dump and the following one (referred to as non-homologous case).

As a sanity check, we compared the results between homologous and non-homologous cases. We expected a shorter cooling time-scale, on average, in the non-homologous case between $\simeq 2500$ days and $\simeq 5000$ days, due to the faster temperature decrease (panel b of figure 6 in Iaconi et al. 2019). We do observe such a feature and, at its maximum, the difference in cooling time-scale between the two cases is about a factor of two. This mainly leads to the formation of a larger number of smaller dust grains in the non-homologous case. Nevertheless, we would not expect a large

difference in the location of the photosphere because the radius and temperature of the photosphere do not depend greatly on the grain radius so long as it is less than $0.1 \mu\text{m}$ (Iaconi et al. 2019).

3 DUST FORMATION PROCESS

In Figure 1 we plot Λ_{on} as a function of the distance from the center of mass (CoM) of the system and for both types of dust considered in this work. The particles shown in each panel are only those that have achieved the condition for the onset of dust formation ($S \geq 10$) before the time at which each snapshot is taken. We plot these quantities at four different times: the end of the dynamic in-spiral ($\simeq 300$ days), the end of the formation of the outer dust population ($\simeq 900$ days; see below and Section 4.2), the onset of homologous expansion in the ejecta ($\simeq 5000$ days) and the end of the simulation (18434 days). Additionally, we show as a colour gradient the onset time of dust formation, t_{on} , of the SPH particles. For the great majority of the particles, the values of Λ_{on} we record at t_{on} are larger than unity (in Figure 1 all the SPH particles for C grains and most of them for MgSiO_3 grains, respectively, reside above the black horizontal line). This means that, for the great majority of the particles, the nucleated seed clusters can grow stably through the accretion of the key gas species. Therefore, nearly the maximum possible amount of dust is formed in our simulation. The difference in the values of Λ_{on} between the two dust types mainly stems from the difference in condensation temperature and number abundance of the key gas species.

We observe two distinct populations for Λ_{on} : an outer population represented by the diagonal strip formed between $\simeq 300$ and $\simeq 900$ days in the outer layer and an inner population formed by the clump that forms in the inner layers starting from $\simeq 900$ days. We will analyse the two populations in detail in Sections 4.2 and 4.3, when discussing the locations where dust forms and the grain size distribution.

In the outer dust population, the formation of grains mostly proceeds from the outside to the inside of the ejecta. We notice however that, at every fixed distance, dust forms at different times. For example, by picking a distance of 800 AU in Figure 1 (panel (d)), we can see that the colour changes from blue in the upper part of the distribution of each dust type to green in the lower part, which corresponds to a spread in time of $\simeq 900$ days. In the inner dust population, we observe instead a much larger spread of t_{on} at a fixed distance. For example, if we consider a distance of 400 AU in Figure 1 (panel (d)), the range of t_{on} is of the order of several thousands of days. Therefore, especially for the inner dust population, in areas equidistant from the CoM coexist dusty and dust-free regions. This is due to the complex dynamic and thermodynamic interactions taking place in the inner portions of the ejecta even after the dynamic in-spiral (Iaconi et al. 2019).

To show more clearly how t_{on} changes depending on the location inside the ejecta, in Figure 2 we plot the projections on the x-y (panel (a)) and x-z (panel (b)) planes of the SPH particles that formed C grains at 18434 days, where the colour scale represents t_{on} . The results for MgSiO_3 are very similar to those for C and we do not show them. In the projections it is clear that the outer portion of the ejecta has a more evident t_{on} gradient, while the inner region has a more mixed t_{on} distribution.

The process of dust formation, which starts right after the completion of the dynamic in-spiral, lasts until $\simeq 5000$ days. This corresponds to the time required for the ejecta to achieve homologous expansion (Iaconi et al. 2019). At $\simeq 5000$ days $\simeq 96\%$

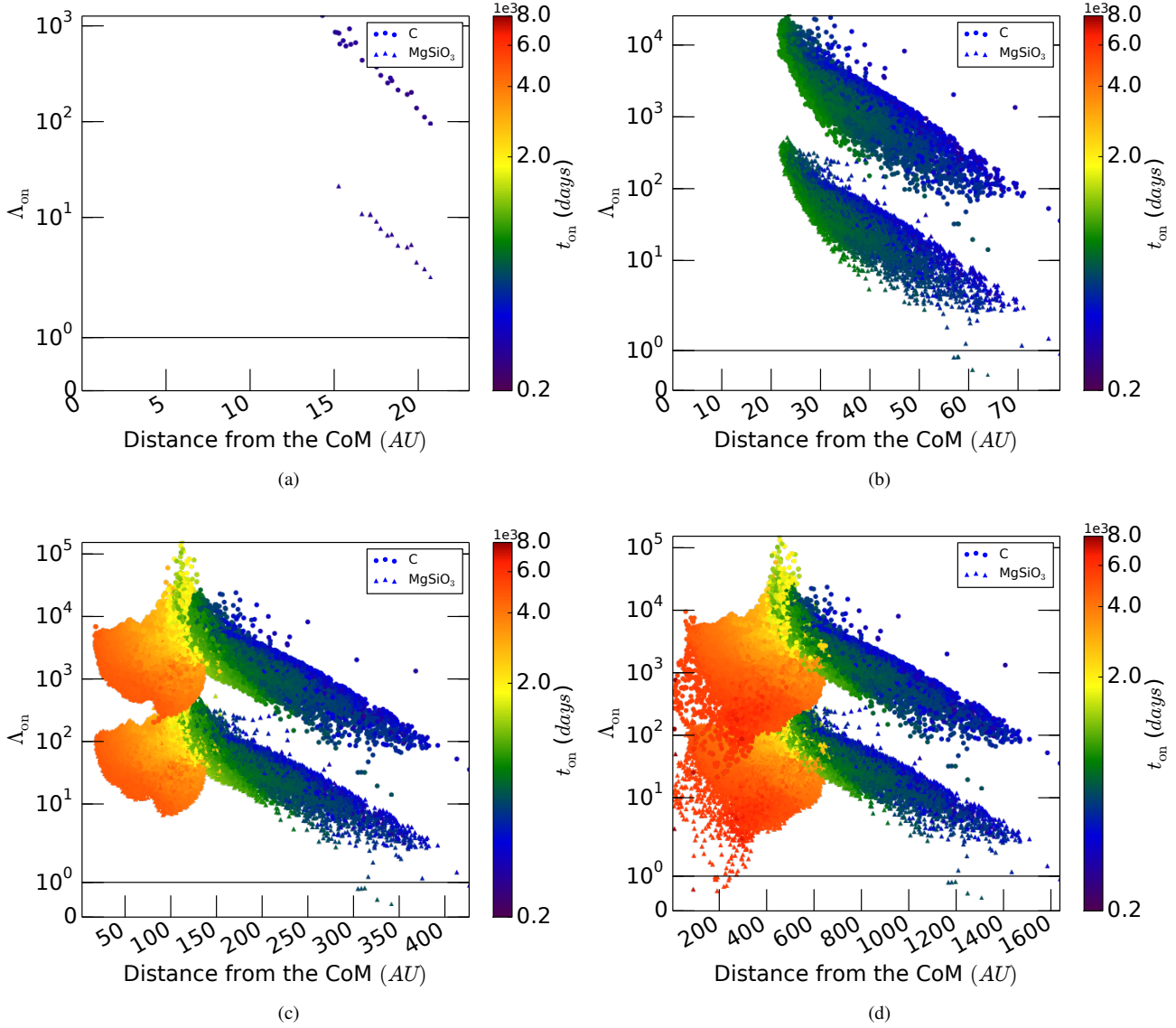


Figure 1. Λ_{on} for the particles that have achieved the condition $S \geq 10$ as a function of the distance from the CoM of the system, at $\simeq 300$ days (a), $\simeq 900$ days (b), $\simeq 5000$ days (c) and 18434 days (d) for C and MgSiO_3 grains. The colour scale represents t_{on} , while the black horizontal line represents $\Lambda_{\text{on}} = 1$.

and $\simeq 97\%$ of the particles, for MgSiO_3 and C, respectively, have formed dust. Most of the remaining particles slowly form dust over the remaining $\simeq 15\,000$ days of the simulation. The fact that the dust formation process starts at the end of the dynamic in-spiral and terminates when the ejecta achieve homologous expansion is purely coincidental.

4 CHARACTERISTICS OF THE DUST

The model proposed by Nozawa & Kozasa (2013) allows us to evaluate several properties of the newly formed dust. In this section we will analyse these properties and their implications.

4.1 Average grain size

Let us first consider the evolution of the average grain radius, a_{ave} , as a function of time (Figure 3). For both MgSiO_3 and C grains we observe a general increase in a_{ave} during the first $\simeq 2500$ days of the simulation. This is followed by a small decrease up to $\simeq 5000$ days, when all the possible dust grains have formed (Section 3) and a_{ave} becomes constant.

Larger grains form on average at later times. In the model we use, a_{ave} is roughly proportional to $\Lambda_{\text{on}} \propto \rho_{\text{on}} T_{\text{on}}^{3/2}$ (but see equation 64 of Nozawa & Kozasa 2013 for the correct relationship), where ρ_{on} is the density of an SPH particle at the onset of dust formation and T_{on} is its temperature (equations 63 and 64 of Nozawa & Kozasa 2013). Hence an increase in the average grain size means that dust grains form in denser layers of the ejecta at later times. In Figure 1 (panel (d)) we observe that, within 600 AU from the CoM of the system, the maximum value of Λ_{on} is approx-

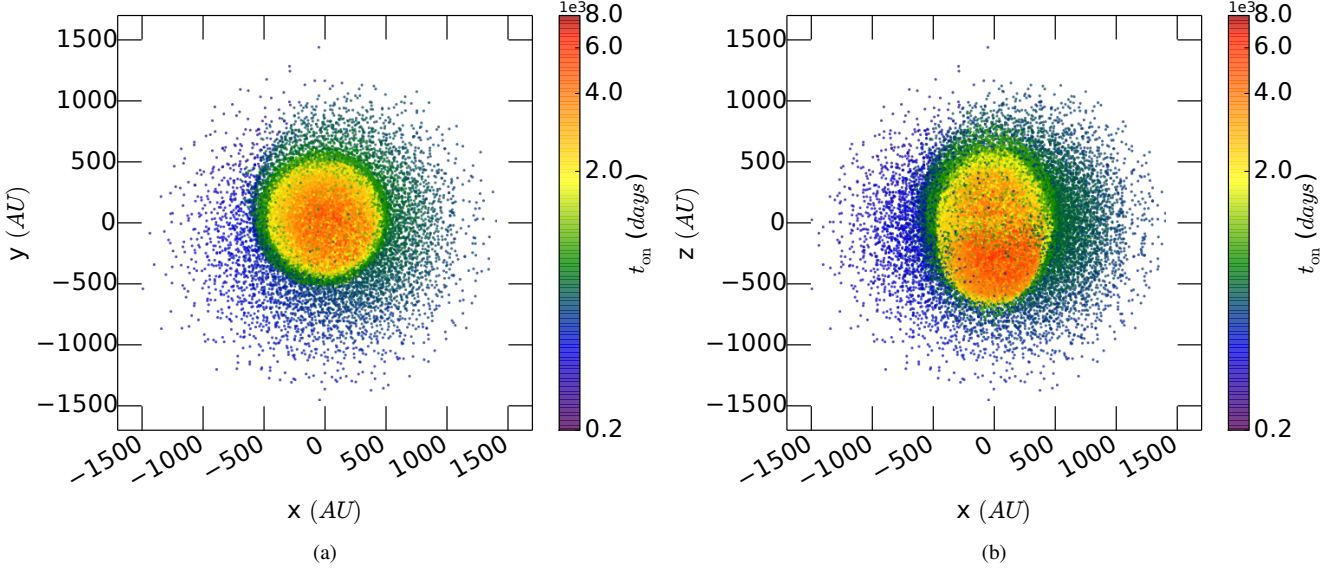


Figure 2. Projections on the $x - y$ (panel a) and $x - z$ (panel b) planes of the SPH particles that formed C grains, t_{on} is represented by the colour scale. The projections are taken at 18434 days, the end of the simulation. The results for MgSiO_3 grains are very similar to those showed here.

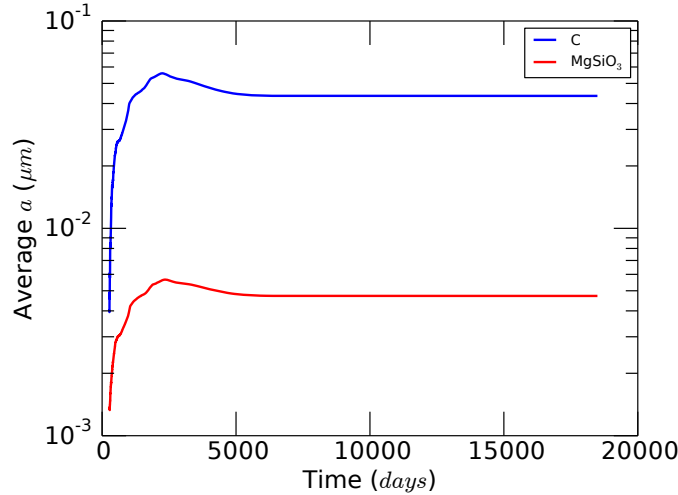


Figure 3. Average grain size, a_{ave} , for MgSiO_3 and C dust as a function of time.

imately constant. This region becomes populated between 900 and 5000 days. A constant maximum Λ_{on} results in a constant maximum grain size. As a result the values of a_{ave} change only depending on the amount and size of smaller dust grains. The increase in number of smaller grains between 900 and 5000 days reduces the value of a_{ave} and produces the small bump we observe after the initial steady increase.

The difference in average radius between C and MgSiO_3 grains is instead dictated by the different number densities of the key elements of the two dust types, C and MgSiO_3 , respectively. The former has a higher number density, resulting in a final $a_{\text{ave}} \simeq 4 \times 10^{-2} \mu\text{m}$, while the latter has a lower one, and a final $a_{\text{ave}} \simeq 5 \times 10^{-3} \mu\text{m}$.

4.2 Location of the grains

By looking at the distribution of grains with respect to the CoM of the system (Figure 4) we can see two distinct populations. The outer dust population is composed by the grains that form earlier and shows a decreasing grain size at increasing distance from the CoM. In Figure 4 the outer population can be identified with the blue to green points that occupy the area between $\simeq 600$ AU and $\simeq 1600$ AU from the CoM. The inner dust population is instead formed by the grains residing at distances < 600 AU. The two populations form from $\simeq 300$ to $\simeq 900$ days (outer population) and $\simeq 900$ to $\simeq 5000$ days (inner population), and can be correlated with the shapes of the profiles of temperature and density of the ejecta. At the end of the simulation we in fact observe that the region between $\simeq 600$ AU and $\simeq 1600$ AU corresponds to a region where temperature and density decrease at increasing distance from the CoM (for the density plot, see figure 3 of Iaconi et al. 2019).

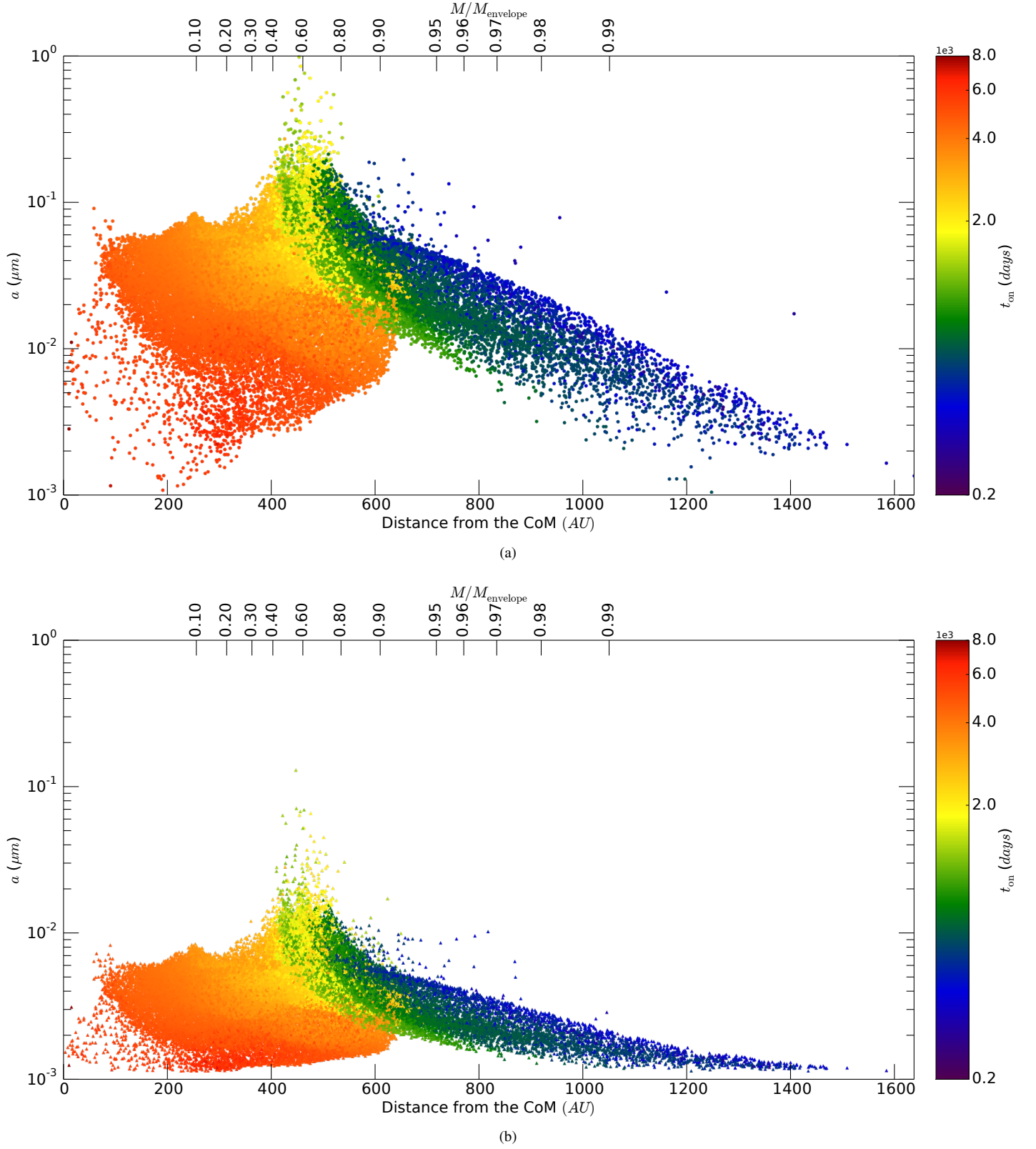


Figure 4. Grain radius, a , as a function of the distance from the CoM of the system for C (a) and MgSiO_3 (b) grains at the end of the simulation. On the upper x axis we plot the mass coordinate with respect to the total ejecta mass. The colour scale represents t_{on} .

The formation of two populations is due to the envelope ejection dynamics. The SPH particles that produce the outer dust population amount to $\simeq 10\%$ of the ejecta mass and coincide to the part of the ejecta that is unbound purely by being accelerated above escape velocity by the deposited orbital energy (Iaconi et al. 2017, Iaconi et al. 2018). This part of the ejecta cools down almost adiabatically after being unbound, because it is free to expand into the empty space. As a result the gas temperature decreases until it reaches values suitable for dust formation at earlier times than in the remaining part of the ejecta.

The inner layers of the ejecta strongly interact with each other in the course of the first $\simeq 5000$ days of the simulation (Iaconi et al. 2019). This results in a more complex evolution and produces the inner dust population whose formation time and size are diverse. For both populations, but more so for the second one, grains of different sizes form at different times for a given distance from the centre. This is reminiscent of the behaviour of Λ_{on} . In fact, in accordance to the formulation of Nozawa & Kozasa (2013), $a_{\text{ave}} \propto \Lambda_{\text{on}} \propto \tau_{\text{sat}}(t_{\text{on}})/\tau_{\text{coll}}(t_{\text{on}})$. Therefore, the size of the grains that form in a specific SPH particle depends on the balance between how fast the new seed nuclei form (τ_{sat}) and how fast the gas particles can collide with the seed nuclei and pre-formed grains to grow them (τ_{coll}). The combination of large τ_{sat} and small τ_{coll} results in a rapid build up of large grains. As a result, we observe that, at the same distance from the CoM, SPH particles form larger grains at earlier times as well as smaller grains at later times (see also Section 4.1). This process takes place roughly in two phases. First, a front of dust formation, starting from the outskirts of the ejecta, moves inwards and forms the larger grains. At this point, in the inner layers of the ejecta we have SPH particles where larger dust grains have already formed and SPH particles where the gas has not yet met the physical conditions for dust formation. The latter are where the smaller dust grains are gradually formed. This process is clear by looking at the distribution of the colours in Figure 4.

When dust starts forming after the dynamic in-spiral, at $\simeq 300$ days, the first grains form at $\simeq 20$ AU from the CoM of the binary. By $\simeq 5000$ days the dust stops forming. The last grains form at $\simeq 100$ AU. Therefore, we observe dust forming roughly in a 100 AU shell around the binary system. Previous results on dust formation in CE (Lü et al. 2013) using a 1D model, estimated a range between $\simeq 7$ and 7×10^4 AU, much larger than the one we obtain here, implying that their ejecta rarefy and cool down more slowly in the 1D model than in our 3D model.

4.3 Grain size distribution

For both the dust types considered, the size distributions are weighted towards small grains. They peak at $\simeq 3 \times 10^{-3} \mu\text{m}$ for C and $\simeq 1.8 \times 10^{-3} \mu\text{m}$ for MgSiO_3 grains. Moreover, we can see that the size of the grains spans a relatively broad range, between $\simeq 3 \times 10^{-3}$ and $\simeq 9 \times 10^{-1} \mu\text{m}$ for C and between $\simeq 1.4 \times 10^{-3}$ and $\simeq 7 \times 10^{-2} \mu\text{m}$ for MgSiO_3 . This is shown in Figure 5, where we plot the number of dust grains vs. the grain radius, a for C (panel (a)) and MgSiO_3 (panel (b)).

We observe that the distributions have a distinct shape, with a net change of slope at $\simeq 5 \times 10^{-2} \mu\text{m}$ and $\simeq 5 \times 10^{-3} \mu\text{m}$ for C and MgSiO_3 grains, respectively. This turnover point, in terms of how much ejecta mass is contained in a single Δa bin, represents the average grain size. In other words, the Δa bins around the turnover point are those that contain the highest amount of gas mass per number of dust grains. We can match the turnover point in

grain size with the maximum in the density distribution of SPH particles (Figure 6), located at $\simeq 7 \times 10^{-16} \text{ g cm}^{-3}$. By looking at the dotted lines in the two panels of Figure 5, that represent constant masses, it is possible to see that on the left of the turnover points, the magenta lines move closer to the constant mass lines, while on the right of the turnover points the cyan lines moves closer to the constant mass lines. A similar behaviour can be observed for the maximum of the density distribution in Figure 6. This informs us of the fact that a turnover point in density results in a turnover point in the grain size distribution.

We are able to fit two power laws through the data, marked by the magenta and cyan lines in Figure 5. The two power laws have been fit through the data between the vertical dashed lines and the fitting parameters are shown in Table 1, where for the power law we use the nomenclature $n(a) = Ca^{-q}$, the same as that of Nozawa (2016). Let us now consider separately the three areas of Figure 5 separated by the vertical dashed lines.

The left side of the distribution, with the smallest grains formed at very low densities in the late stages of the dust formation (see, e.g., Figure 4), does not display any particular trend. The gas where these grains are located achieves homologous expansion after dust is formed, i.e., after $\simeq 5000$ days from the beginning of the simulation. We highlight that, even though the number of dust grains in this part of the distribution is large, the mass of the gas where they reside, and hence the dust mass, is quite low. Its mass corresponds to $\simeq 0.44\%$ and $\simeq 1.32\%$ of the ejecta mass for C and MgSiO_3 , respectively. This is in line with the results obtained by Iaconi et al. (2019), who showed that most of the ejecta has achieved homologous expansion by the $\simeq 5000$ days mark.

The middle part of the distributions contain the majority of the ejecta mass, $\simeq 67\%$ in the case of C grains and 61% in the case of MgSiO_3 grains. The power law slopes representing the distribution are -1.62 and -1.43 , for C and MgSiO_3 , respectively. All of these dust grains form in areas where the gas has already achieved homologous expansion. We highlight here that we performed the fit in logarithmic space, i.e., on the distribution obtained as $n(a) = dn/d \log a$, where n is the number of dust grains. As a result the slopes of the power law fits decrease by 1 if the distribution is fitted in linear space¹, resulting in exponents of -2.62 and -2.43 . The linear slopes we obtain differ from the typical values estimated for interstellar dust grains, which are in the range $-3.5 \lesssim -q \lesssim -4$ (e.g., Nozawa & Fukugita 2013).

The right part of the distributions corresponds to the cusps pointing upward visible in Figure 4 and also in this case the dust grains form in regions where the gas has achieved homologous expansion. The cusps are located between $\simeq 300$ and $\simeq 600$ AU for both C and MgSiO_3 and contain, respectively, $\simeq 32\%$ and $\simeq 37\%$ of the ejecta mass. This part of the distributions are fitted by power law whose slopes are steeper than for smaller grains with exponents of -6.56 and -6.67 , for C and MgSiO_3 , respectively. These exponents correspond to -7.56 and -7.67 for a linear fit. Also in this case the linear slopes we obtain differ from the typical values estimated for interstellar dust grains. The presence of a steeper power law at larger grain size is a feature which appears also in other dust formation environments. For example, Nozawa et al. (2003) observe a crossover point between smaller and larger grain sizes, with

¹ Let us define the distribution derived in linear space as $\frac{dn}{da}$. This distribution and the one derived in logarithmic space are connected by the relation $\frac{dn}{da} = \frac{1}{a \ln 10} \frac{dn}{d \log a}$. If the distribution derived in logarithmic space is a power law of the type Ca^{-q} , we obtain $\frac{dn}{da} = \frac{Ca^{-(q+1)}}{\ln 10}$.

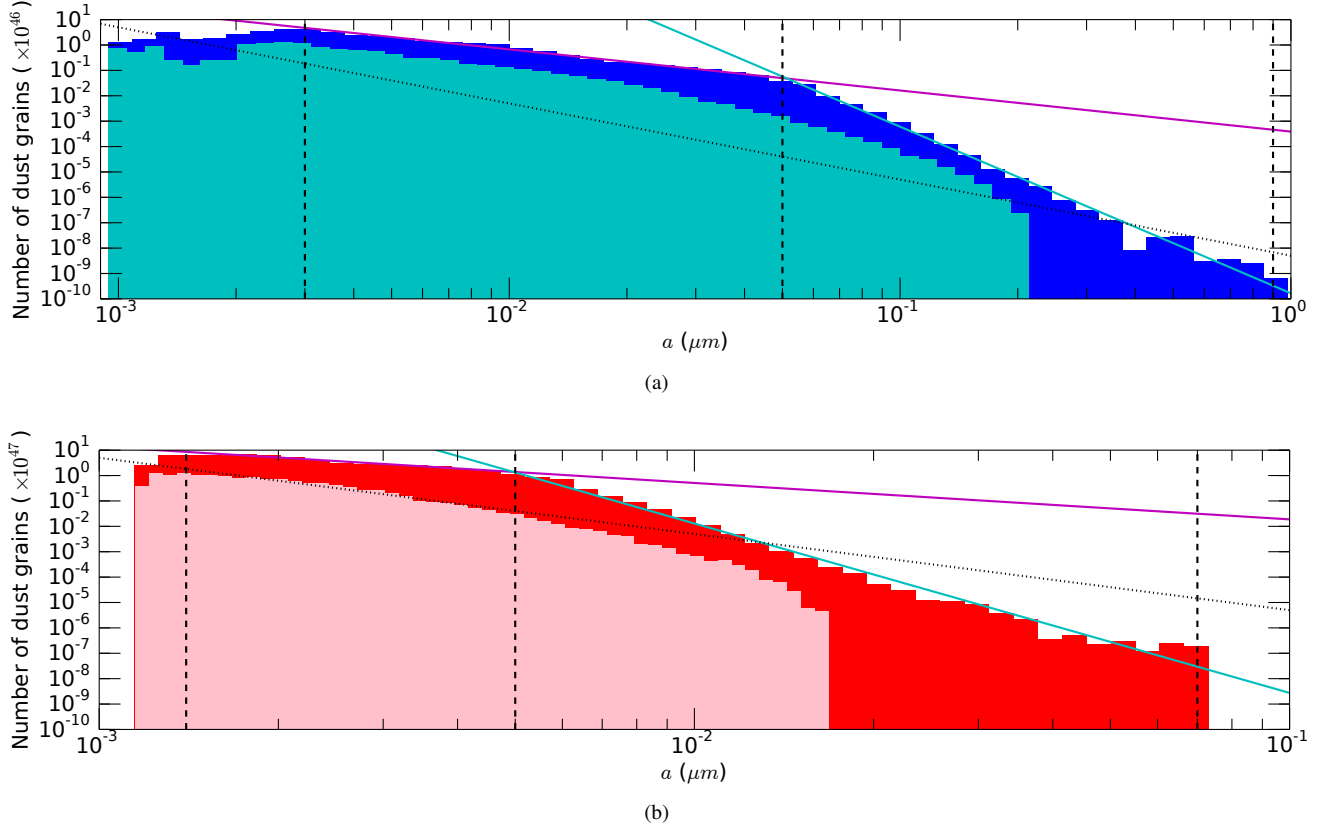


Figure 5. Number of dust grains as a function of the grain radius, a , at the end of the simulation for C grains (a) and MgSiO_3 grains (b). In panel (a) the magenta line represents the best fit to a power law in the range $3 \times 10^{-3} \leq a < 5 \times 10^{-2} \mu\text{m}$, the cyan line in the range $5 \times 10^{-2} \leq a \leq 9 \times 10^{-1} \mu\text{m}$. In panel (b) the magenta line represents the best fit to a power law in the range $1.4 \times 10^{-3} \leq a < 5 \times 10^{-3} \mu\text{m}$, the cyan line in the range $5 \times 10^{-3} \leq a \leq 7 \times 10^{-2} \mu\text{m}$. The boundaries of the fitting are marked by the vertical dashed lines, while the dotted line represents a line at constant mass for reference. We overplot the distribution for the outer dust population (i.e., at 900 days) in cyan (a) and pink (b), for C and MgSiO_3 , respectively. Note that the bin size use for the outer dust population is smaller than that used for the data at the end of the simulation.

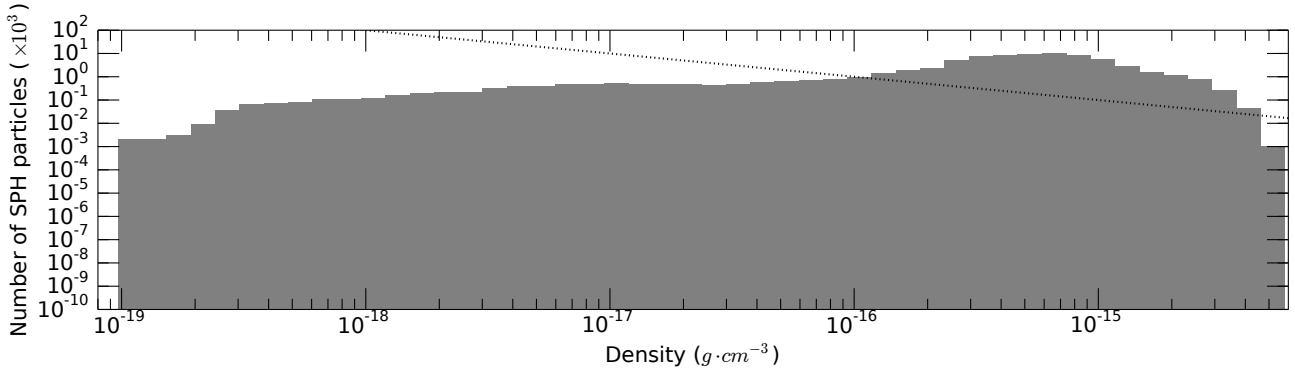


Figure 6. Number of SPH particles as a function of density at the end of the simulation. The dotted line represents a line at constant mass for reference.

a steeper slope for larger grain sizes, for dust formed in supernova ejecta. As mentioned in Section 4.2, the radius of newly formed grains is mainly determined by the gas density at the onset of dust formation; larger dust grains form in denser gas, and vice versa. Hence, the grain size distributions given here reflects more or less the density distribution of SPH particles. This implies that different dynamical models would result in different power-law indices.

We also overplot the distribution for the outer dust in the case of C in cyan (Figure 5, panel (a)) and in the case of MgSiO_3 in pink

(Figure 5, panel (b)), to those of the distribution at the end of the simulation for comparison. The second dust population dominates the grain size distribution at the end of the simulation. This is particularly true for large grain sizes. Larger grains are in fact mostly formed in the inner dust population, so the outer population misses that part of the statistic.

Dust type	Magenta			Cyan		
	parameters		std deviation	parameters		std deviation
C	$C = 3.88 \times 10^{-4}$	\pm	6.71×10^{-5}	$C = 1.65 \times 10^{-10}$	\pm	5.55×10^{-11}
	$q = 1.62$	\pm	3.87×10^{-2}	$q = 6.56$	\pm	1.92×10^{-1}
MgSiO ₃	$C = 6.92 \times 10^{-4}$	\pm	4.14×10^{-4}	$C = 5.81 \times 10^{-16}$	\pm	3.92×10^{-16}
	$q = 1.43$	\pm	10^{-1}	$q = 6.67$	\pm	1.68×10^{-1}

Table 1. Parameters of the fits in Figure 5. Note that the nomenclature for the parameters has been chosen to be the same as that of Nozawa (2016), who expresses the power law as $n(a) = Ca^{-q}$; see Nozawa (2016) for further details.

4.4 The shape of the dusty ejecta

The two dust populations discussed in Section 4.2 differ mainly because the former, exterior one is more ordered, with smaller grains residing at larger distances. The latter population is instead more chaotic, with a range of grain sizes at all distances. This is visible in the shape of the dusty ejecta, which we show in Figure 7 for the C grains, where the top row are slices on the $x-y$ and $x-z$ planes at $\simeq 900$ days and the bottom row are the same slices at the end of the simulation. We have chosen 900 days and 18 434 days because they highlight well the separation between the two dust populations.

At $\simeq 900$ days we observe that the dusty part of the ejecta is only the external one, leaving a dust-free cavity around the central binary. Such cavity has an elliptic shape and spans an area between 20 and 30 AU just before the inner population starts forming and filling the dust-free space. In agreement with Figure 4, from the outside to the inside, we observe a trend of increasing grain size as a function of the distance. In the innermost area of the dusty gas there is a layer where the largest grains form (clearly visible as a mostly orange coloured area in panels a and b of Figure 7). This results from the compression generated by the first orbit of the companion inside the primary’s envelope. When the gas belonging to the compressed layer cools down to dust formation temperatures, its higher density prompts the formation of larger grains. Moreover, the dust we observe in panels (a) and (b) of Figure 7 is mostly made up of unbound gas as it forms in the portion of the ejecta that is accelerated above escape velocity during the first orbit of the companion (see also Section 4.2).

At the end of the simulation, the gas has rarefied and cooled enough to form dust over the entire ejecta. In panels (c) and (d) of Figure 7 we crop the slices to a distance of 700 AU, roughly corresponding to the transition distance between the first and second dust populations. In panel (c) we observe that the outermost area shows a greater number of larger grains, these are concentrated on the equatorial plane and correspond to those in the cusp between 400 and 600 AU in Figure 4. We also observe the presence of small grains in the most internal region of the ejecta. The remaining portion of the ejecta is occupied by a mixture of different grain sizes. There is a ring-shaped feature between $\simeq 300$ and $\simeq 400$ AU showing larger grain sizes. Since dust has formed over the entire ejecta, the patterns of the dusty ejecta are the same of those of the density distribution, which presents a higher density ring as shown in figures 4 and 5 of Iaconi et al. 2019. A similar behaviour is present in the simulation of Reichardt et al. (2019a), who carried out a common envelope simulation that did not include the effects of dust but which, by virtue of using a tabulated equation of state, could map the opacity in the envelope as a function of time. In their figure 10, top panels, we see a thick high opacity ring at ~ 100 AU from the centre. This ring compares directly to the ring observed in the outer population dust in Figure 7, which sits at ~ 30 AU. When we account for the fact that the snapshot

presented by Reichardt et al. (2019a) are taken at 1840 days, while those in Figure 7 are taken at 900 days (the outward velocity of the early ejecta is approximately 100 km s^{-1} , justifying the different ring sizes). Finally, the dust distribution in the two perpendicular cuts also matches what is seen in the opacity maps of Reichardt et al. (2019a). Equatorially concentrated dust formation will propel different layers of the ejecta at different speeds contributing to their shaping in addition to what the geometry of the common envelope interaction has already imparted to the ejecta.

4.5 Dust mass

In our simulation every particle forms the same amount of either C or MgSiO₃ grains. This is because the amount of dust formed only depends on the key element number density and on the total mass of the SPH particle, with all the SPH particles in the simulation having the same mass. We show the evolution of the dust mass formed in Figure 8.

The mass of C grains at the end of the simulation amounts to $2.22 \times 10^{-3} M_{\odot}$, while that of MgSiO₃ amounts to $9.39 \times 10^{-4} M_{\odot}$. These values correspond to $\simeq 0.5$ percent and $\simeq 0.2$ percent of the ejected envelope mass, respectively. These values are in the same range to those estimated by Lü et al. (2013), who calculated dust masses ranging between $\simeq 10^{-4} M_{\odot}$ and $5 \times 10^{-2} M_{\odot}$ for the bulk of their models. In the models of Reichardt et al. (2019a), approximately $0.06 M_{\odot}$ of gas reside in the high opacity shell where we presume dust is forming, implying a dust mass of $\sim 6 \times 10^{-4} M_{\odot}$, using a gas-to-dust ratio of 100, a value that is in line with what we find here.

In Figure 8, the shape of the curves for C and MgSiO₃ is similar. This is due to the fact that the supersaturation ratio reaches its critical value, $S = 10$, at the same time for both dust types, and when this happens the vast majority of the SPH particles have $\Lambda_{\text{on}} > 1$, forming the maximum amount of dust possible (see Section 3). As a result, the timing of the production of dust is similar.

The dust mass increases monotonically up to $\simeq 5000$ days, so new grains are constantly formed. As discussed previously in Sections 4.1 and 4.2, we observe the layers of the ejecta gradually forming dust as they expand and cool down. From this it follows straight away that the total dust mass is steadily increasing.

4.6 Contribution of CE to cosmic dust

In this section we estimate the CE contribution to the Galactic dust budget. To do so we need to estimate the number of CE events per year and multiply it by the dust yield of each as determined in Section 4.5 ($\simeq 10^{-3} M_{\odot}$ for both C and MgSiO₃ grains).

We can estimate the number of CE events per year for the Milky Way by assuming that they are the same as the rate of luminous red novae, namely $0.1 - 0.2$ events per year (Kochanek et al.

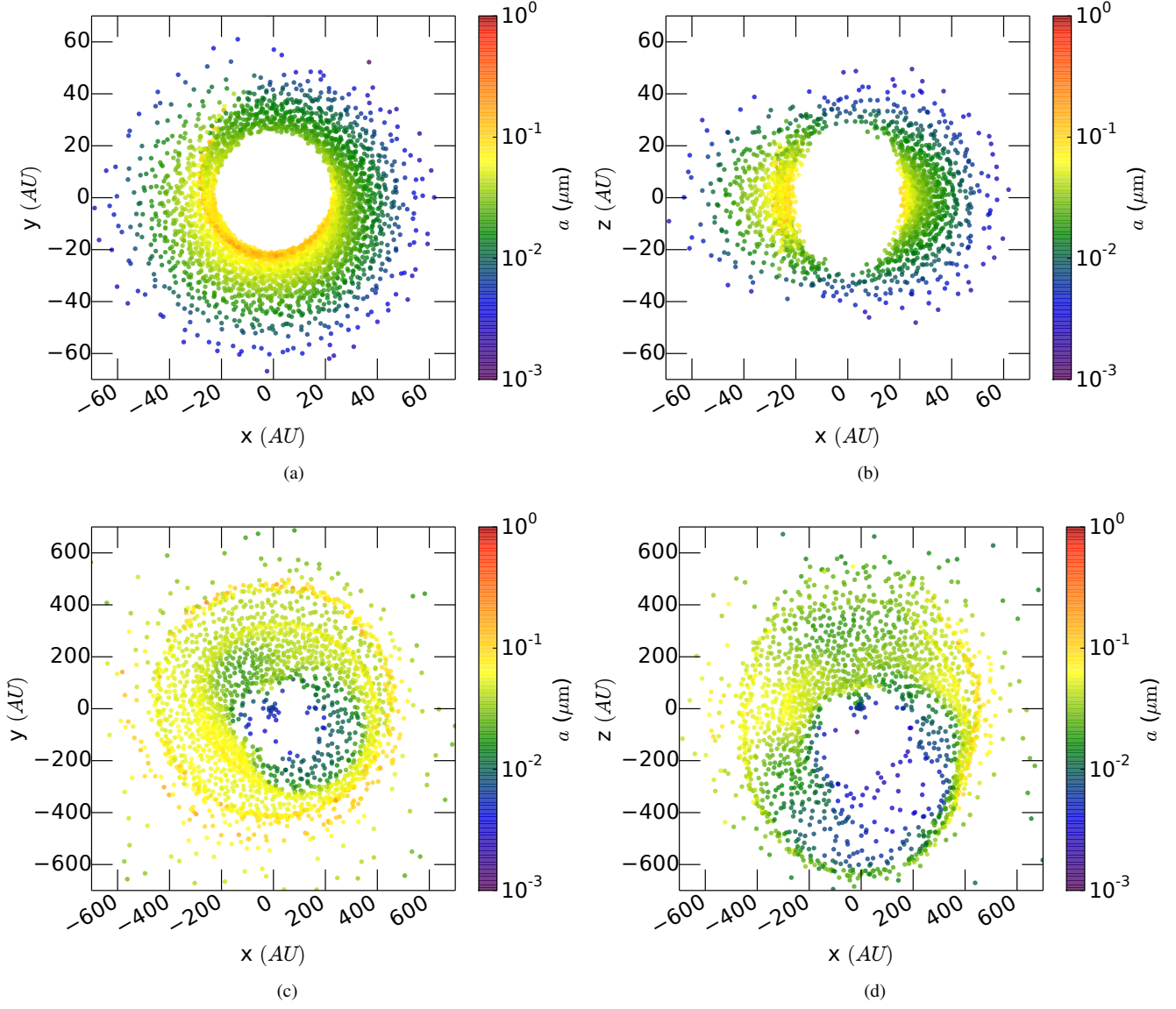


Figure 7. Slices on the $x - y$ (panels (a) and (c)) and $x - z$ (panels (b) and (d)) planes of the SPH particles that formed C grains, the dust size is represented by the colour scale. The slices are taken at $\simeq 900$ days (top) and at 18 434 days (bottom), to clearly show the location of the two dust populations discussed in Section 4.2. Note that panels (c) and (d) are cropped at 700 AU to include only the SPH particles belonging to the inner dust population, formed in the inner regions of the ejecta. We do not plot the map of the MgSiO_3 grains because is very similar to the one of the C grains, only with different grain sizes.

2014, Howitt et al. 2020). We note that this might be an overestimate, because we do not know what percentage of red novae is indeed the result of a CE event. With these numbers we obtain an injection of dust in the ISM by CE events of $1 - 2 \times 10^{-4} \text{ M}_{\odot} \text{ yr}^{-1}$. The dust injected in the ISM by sources other than supernovae or novae, namely all stellar winds, is estimated to be $\sim 4.5 \times 10^{-3} \text{ M}_{\odot} \text{ yr}^{-1}$ for the Milky Way (Draine 2009). The CE contribution to the Galactic dust can therefore be estimated to be up to 5% of the dust produced by other known sources. The estimate provided here gives an idea of the fact that the injection of dust into the ISM by CE does not dominate the cosmic dust production, but might not be negligible and could be comparable to other dust sources such as novae and SNe (see, e.g., table 1 of Draine 2009).

Lü et al. (2013) also considered the Galactic dust production from CE events over the Galaxy’s lifetime using an analytical estimate of the dust production and a population synthesis code to

determine the rate of CE occurrences. They use a dust yield per event similar to ours, and an estimated 20% of all systems that go through a CE interaction, which corresponds to a rate up to 0.8 events per year. As a result of their four times higher frequency of CE interactions, they obtain a larger yield of dust by CE events.

5 OBSERVATIONAL COUNTERPARTS

The number of common envelope events observed is multiplying quickly. Recently, a new class of infrared transients was discovered and initially classified by Jencson et al. (2019) and at least a couple of their still very small sample are similar to other events that, in the optical, have been interpreted as common envelope mergers. It is also clear that in most cases dust is present (Jencson et al. 2019;

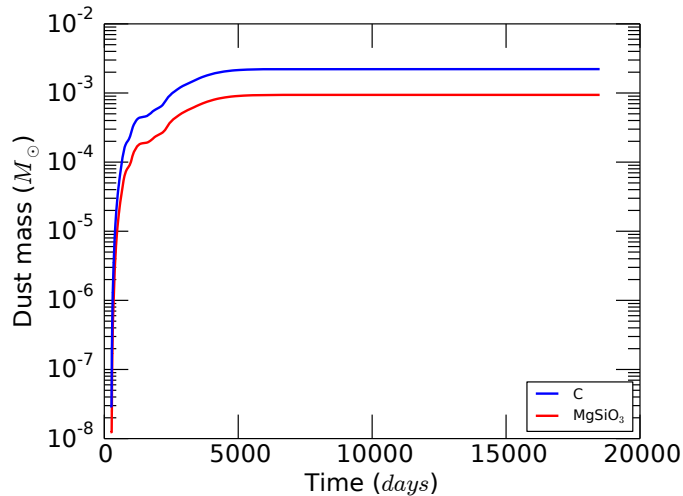


Figure 8. Dust mass formed as a function of time for MgSiO_3 and C grains.

Pastorello et al. 2019). That said, the number of studies of the dust properties is very small.

The only study of the dust properties of what is now recognised to have been a common envelope merger, between a solar mass star and a much less massive companion, is by Nicholls et al. (2013). They analysed dust formation between $\simeq 547$ days and $\simeq 700$ days after the outburst of the CE merger event V1309 Sco (Tylenda et al. 2011). They pointed out that V1309 Sco was undetected in the mid-IR band before its eruption, therefore the dust formation observed was triggered by the CE event.

Nicholls et al. (2013) constructed a simple dust model based on their data. Their model considers a couple of dust species, grain sizes between 0.1 and $4.0 \mu\text{m}$ and temperatures between 200 and 1500 K. Within these ranges they selected the dust type and size that best fit the observational data. They concluded that the continuum is well represented by amorphous silicates dust at 400 K, while the main absorption line can be fitted by amorphous pyroxene dust of $3 \mu\text{m}$ at 800 K. The warm temperature and large grain size indicated by the line feature led them to conclude that the dust has recently formed and was processed in the circumstellar environment, rather than inside the stellar envelope, thus confirming its CE origin.

Our dust formation model is based on a system where the primary has a mass similar to the primary star of V1309 Sco, but is substantially larger and our companion is 4 times more massive (for a range of possible parameters of this system see e.g., Tylenda et al. 2011). Despite these differences we carry out a comparison.

The V1309 Sco merger took place during the very early RGB phase of the primary, so we will be looking at the MgSiO_3 grains for a comparison, a silicate mineral such as the one derived by Nicholls et al. (2013). According to our model, dust would form between $\simeq 300$ and $\simeq 5000$ days from the beginning of the simulation, where $\simeq 300$ days marks the end of the dynamic in-spiral phase. During this period both temperature and density decrease by one order of magnitude in the inner parts of the ejecta to several orders of magnitude in the outskirts. We observe that dust forms as soon as the gas reaches temperatures below 1000 K. Therefore we predict that dust forms in warm environment, similar to the conclusion of Nicholls et al. (2013). On the other hand, the entire MgSiO_3 dust population in our simulation has sizes smaller than $0.1 \mu\text{m}$. It is therefore possible that in our case dust forms at densities low

enough to counter balance the warm temperatures and still produce small grains.

Given the differences and the approximations in our model and in the observation-derived quantities it is impossible to perform an accurate quantitative comparison. However, there are a few points that can be made:

(i) The formation of large dust particles usually requires extreme environments and/or special physical processes (e.g., coagulation via grain-grain collisions). In the current calculation we do not include such processes and therefore, even if a population of larger grains could be formed, we would not be able to reproduce it. Nevertheless, given the typical densities and temperatures of our gas, it seems unlikely that larger grains would be able to form.

(ii) Grain sizes derived from IR-SED fitting tend to be large ($\gtrsim 1 \mu\text{m}$). This is known for the case of nova ejecta, type II SN, AGB stars and PN (Meixner et al. 2002, Wesson et al. 2010, Sakon et al. 2016). Therefore, the study of Nicholls et al. (2013) might be obtaining grain sizes systematically larger than the actual grain population actually present in V1309 Sco.

(iii) Nicholls et al. (2013) concluded that the dust is formed in the post dynamic in-spiral phase. However, there is another possible scenario for the dust formation in V1309 Sco. As can be seen in figure 1 of Nicholls et al. (2013), the optical light curve quickly declines during the year 2007, roughly one year before the outburst. In the phase before the outburst, dust could have formed in gas lost from the binary prior to the dynamic in-spiral. These dust grains could then have been swept up by the material ejected during the dynamic in-spiral and heated up to temperatures high enough to emit in the IR band. In such a scenario, dust can form in physical conditions more suitable for the formations of grains with sizes $\gtrsim 1 \mu\text{m}$.

A more adequate comparison would require more observations of dust in post-CE systems together with more theoretical dust formation models based on CE simulations. These are both missing in the current literature.

6 SUMMARY AND CONCLUSIONS

In this paper, we presented the first work on dust formation based on a 3D hydrodynamic simulation of the CE interaction. We ex-

tended the work carried out by Iaconi et al. (2019) by applying the dust formation model of Nozawa & Kozasa (2013) to the simulation outputs of the 3D SPH hydrodynamic simulation of the CE binary interaction of Iaconi et al. (2019). In this simulation, the system has been evolved for 18 434 days ($\simeq 50$ yr) after the termination of the dynamic in-spiral to assess the dynamic and thermodynamic behaviour of the ejecta. This allows us to investigate the details of the formation of dust, its spatial distribution and its size and to estimate the contribution of the CE interaction on the production of cosmic dust. We consider two types of dust, carbon dust (C) and pyroxene-type silicates dust (MgSiO_3), that represent the most common types of grains present in the interstellar dust. Our main results are the following:

(i) In both cases of C and MgSiO_3 , dust grains are produced all over the ejected envelope (i.e., in 99% of the SPH particles). The dust formation starts right after the end of the dynamic in-spiral ($\simeq 300$ days) and terminates at $\simeq 5000$ days.

(ii) The dust formed can be divided into two populations, an outer one formed between $\simeq 300$ and $\simeq 900$ days, and an inner one formed between $\simeq 900$ and $\simeq 5000$ days from the rest of the ejecta. In the outer population dust is formed in a more ordered way with respect to the inner population, starting at larger distances and with smaller grains and terminating at smaller distances with larger grains. The inner population is more complex, with multiple grain sizes forming in the same layers at different times. The formation of two populations is the result of different envelope ejection dynamics. The outer population is formed in the gas that belongs to the outer layers of the primary, which are rapidly unbound during the first orbit of the companion inside the CE and expand with negligible self-interaction in the empty space around the binary. The inner population is formed in the gas that belongs to the inner layers of the primary; such layers strongly interact with one another, achieving the conditions for dust formation under different combinations of physical parameters inside the same layer.

(iii) On average, the size of dust grains formed increases as time passes. At the end of the dust formation process the average radius of the grains is $\simeq 4 \times 10^{-2} \mu\text{m}$ for C and $\simeq 5 \times 10^{-3} \mu\text{m}$ for MgSiO_3 .

(iv) For both C and MgSiO_3 the size distribution of the dust formed is weighted towards small grains and spans a relatively broad range. The distributions can be fitted with a double power law, with a turnover point where the slope of the fitting power law changes. The power law fitting the smaller grain sizes is flatter than the one for the larger grain sizes, a feature present also in other astrophysical environments such as supernovae (Nozawa et al. 2003). However, the indexes of the two power laws differ from the canonical value expected for the interstellar dust grains. To better clarify what is happening, the same dust formation calculation should be carried out for several CE simulations. This would allow us to see, e.g., whether this is a common feature of different CE systems.

(v) The mass of the dust formed in the ejecta is $\simeq 10^{-3} M_\odot$ for both C and MgSiO_3 . By assuming this value as a standard dust yield from CE interactions we estimated the contribution of CE to cosmic dust to be $1 - 2 \times 10^{-4} M_\odot \text{ yr}^{-1}$, or $\simeq 5\%$ of that produced by main dust sources, i.e., stellar winds. Such a contribution is not dominant but non negligible, and comparable to that of novae and SNe.

(vi) A comparison with an observational study on dust formation in the post-CE merger V1309 Sco by Nicholls et al. (2013) shows that we have quite different results in terms of the grain sizes obtained, with our grains being much smaller than those esti-

mated from the observations. However, there are several caveats in both our theoretical work and the procedure used by Nicholls et al. (2013) which make a comparison very difficult.

This is the first work on dust formation based on a 3D hydrodynamic simulation of the CE interaction. We hope that in the future more work of this kind will be performed with different stellar masses, orbital parameters, dust formation models and numerical codes to achieve a deeper understanding of the dust formation process during the CE evolution.

ACKNOWLEDGMENTS

RI is grateful for the financial support provided by the Postdoctoral Research Fellowship of the Japan Society for the Promotion of Science (JSPS P18753). KM acknowledges the support provided by the JSPS KAKENHI grant 18H04585, 18H05223, and 17H02864. TN acknowledges the support provided by the JSPS KAKENHI grant 18K03707. We acknowledge the computational facilities of the Department of Physics and Astronomy of Macquarie University, on which the simulations have been carried out. The computations described in this work were performed using the PHANTOM code (<https://phantomsp.bitbucket.io/>), which is the product of a collaborative effort of scientists under the lead of A/Prof. Daniel Price (Monash University, Melbourne, VIC, Australia). All simulation outputs are available upon request by e-mailing roberto.iaconi@kusastro.kyoto-u.ac.jp.

REFERENCES

- Asplund, M., Grevesse, N., Sauval, A. J., & Scott, P. 2009, *Annual Review of Astronomy and Astrophysics*, 47, 481
- Clayton, D. D., Liu, W., & Dalgarno, A. 1999, *Science*, 283, 1290
- Clayton, M., Podsiadlowski, P., Ivanova, N., & Justham, S. 2017, *MNRAS*, 470, 1788
- De, S., MacLeod, M., Everson, R. W., et al. 2019, arXiv e-prints, arXiv:1910.13333
- Draine, B. T. 2009, in *Astronomical Society of the Pacific Conference Series*, Vol. 414, *Cosmic Dust - Near and Far*, ed. T. Henning, E. Grün, & J. Steinacker (Astronomical Society of the Pacific), 453
- Evans, A., Tyne, V. H., Smith, O., et al. 2005, *MNRAS*, 360, 1483
- Ferrarotti, A. S. & Gail, H. P. 2006, *A&A*, 447, 553
- Glanz, H. & Perets, H. B. 2018, *MNRAS*, 478, L12
- Howitt, G., Stevenson, S., Vigna-Gómez, A. r., et al. 2020, *MNRAS*, 30
- Iaconi, R. & De Marco, O. 2019, *MNRAS*, 490, 2550
- Iaconi, R., De Marco, O., Passy, J.-C., & Staff, J. 2018, *MNRAS*, 477, 2349
- Iaconi, R., Maeda, K., De Marco, O., Nozawa, T., & Reichardt, T. 2019, *MNRAS*, 489, 3334
- Iaconi, R., Reichardt, T., Staff, J., et al. 2017, *MNRAS*, 464, 4028
- Ivanova, N. 2018, *ApJ*, 858, L24
- Ivanova, N., Justham, S., Chen, X., et al. 2013, *The Astronomy and Astrophysics Review*, 21, 59
- Ivanova, N. & Nandez, J. L. A. 2016, *MNRAS*, 462, 362
- Jencson, J. E., Adams, S. M., Bond, H. E., et al. 2019, *ApJ*, 880, L20
- Kochanek, C. S., Adams, S. M., & Belczynski, K. 2014, *MNRAS*, 443, 1319

- Kuruwita, R. L., Staff, J., & De Marco, O. 2016, MNRAS, 461, 486
- López-Cámara, D., De Colle, F., & Moreno Méndez, E. 2019, MNRAS, 482, 3646
- Lü, G., Zhu, C., & Podsiadlowski, P. 2013, ApJ, 768, 193
- MacLeod, M., Antoni, A., Murguía-Berthier, A., Macías, P., & Ramírez-Ruiz, E. 2017, ApJ, 838, 56
- Meixner, M., Ueta, T., Bobrowsky, M., & Speck, A. 2002, ApJ, 571, 936
- Murguía-Berthier, A., MacLeod, M., Ramírez-Ruiz, E., Antoni, A., & Macías, P. 2017, ApJ, 845, 173
- Nandez, J. L. A. & Ivanova, N. 2016, MNRAS, 460, 3992
- Nandez, J. L. A., Ivanova, N., & Lombardi, J. C. 2015, MNRAS, 450, L39
- Nicholls, C. P., Melis, C., Soszynski, I., et al. 2013, MNRAS, 431, L33
- Nozawa, T. 2016, Planetary and Space Science, 133, 36
- Nozawa, T. & Fukugita, M. 2013, ApJ, 770, 27
- Nozawa, T. & Kozasa, T. 2013, ApJ, 776, 24
- Nozawa, T., Kozasa, T., Umeda, H., Maeda, K., & Nomoto, K. 2003, ApJ, 598, 785
- Ohlmann, S. T., Röpke, F. K., Pakmor, R., & Springel, V. 2016a, ApJ, 816, L9
- Ohlmann, S. T., Röpke, F. K., Pakmor, R., Springel, V., & Müller, E. 2016b, MNRAS, 462, L121
- Paczynski, B. 1976, in IAU Symposium, Vol. 73, Structure and Evolution of Close Binary Systems, ed. P. Eggleton, S. Mitton, & J. Whelan, 75
- Passy, J.-C., De Marco, O., Fryer, C. L., et al. 2012, ApJ, 744, 52
- Pastorello, A., Chen, T. W., Cai, Y. Z., et al. 2019, A&A, 625, L8
- Reichardt, T., De Marco, O., Iaconi, R., & Price, D. 2019a, arXiv e-prints, arXiv:1911.02759
- Reichardt, T. A., De Marco, O., Iaconi, R., Tout, C. A., & Price, D. J. 2019b, MNRAS, 484, 631
- Ricker, P. M. & Taam, R. E. 2012, ApJ, 746, 74
- Sakon, I., Sako, S., Onaka, T., et al. 2016, ApJ, 817, 145
- Sandquist, E. L., Taam, R. E., Chen, X., Bodenheimer, P., & Burkert, A. 1998, ApJ, 500, 909
- Schreier, R., Hillel, S., & Soker, N. 2019, MNRAS, 490, 4748
- Shiber, S., Iaconi, R., De Marco, O., & Soker, N. 2019, MNRAS, 488, 5615
- Shiber, S., Kashi, A., & Soker, N. 2017, MNRAS, 465, L54
- Shiber, S. & Soker, N. 2018, MNRAS, 477, 2584
- Soker, N., Grichener, A., & Sabach, E. 2018, ApJ, 863, L14
- Staff, J. E., De Marco, O., Macdonald, D., et al. 2016, MNRAS, 455, 3511
- Tylenda, R., Hajduk, M., Kamiński, T., et al. 2011, A&A, 528, A114
- Wesson, R., Barlow, M. J., Ercolano, B., et al. 2010, MNRAS, 403, 474
- Wilson, E. C. & Nordhaus, J. 2019, MNRAS, 485, 4492